



A laboratory study of internal gravity waves incident upon slopes with varying surface roughness

Yu-Hao He^{1,2}, Bu-Ying-Chao Cheng² and Ke-Qing Xia^{1,2,3,†}

¹Center for Complex Flows and Soft Matter Research and Department of Mechanics and Aerospace Engineering, Southern University of Science and Technology, Shenzhen 518055, PR China

²Department of Physics, The Chinese University of Hong Kong, Hong Kong, PR China

³Guangdong Provincial Key Laboratory of Turbulence Research and Applications, Southern University of Science and Technology, Shenzhen 518055, PR China

(Received 16 September 2021; revised 6 March 2022; accepted 20 April 2022)

We report a laboratory study on the scattering, energy dissipation and mean flow induced by internal gravity waves incident upon slopes with varying surface roughness. The experiment was performed in a rectangular box filled with thermally stratified water. The roughness of the slope surface, λ , defined as the height of a roughness element over its base width, and the off-criticality $\gamma = (\alpha - \beta)/\beta$, with α and β being the angles of the incident wave and the slope, are used as two control parameters. The distribution of energy dissipation in the direction normal to the slope is found to be more uniform in the rough surface cases. Counter-intuitively, both the maximum value in the dissipation profile and the total energy dissipation near the slope are reduced by surface roughness under most circumstances. The measured peak width (the full width at half-maximum of the peaks) of the dissipation profile is found to be broadened significantly in the rough surface cases. We also observed that there exists a non-zero optimal off-criticality ($\gamma = 0.17$ for the present measurement resolution) for the normalized average dissipation and total dissipation, which may be due to the strongest wave energy near the slope at this γ . Unlike surface roughness, the off-criticality has a small effect on the distribution of energy dissipation. Moreover, surface roughness is also found to change the structure of the scattering-induced mean flow and enhance its strength. The present study provides new perspectives on how the surface roughness on topographic features influences energy dissipation.

Key words: internal waves, topographic effects

† Email address for correspondence: xiakq@sustech.edu.cn

1. Introduction

Oceanic internal gravity waves, which are generated mainly by winds near the ocean surface or tidal flow over bottom topographies, are thought to provide a large amount of energy to sustain the ocean mixing when they break and dissipate (see e.g. Munk & Wunsch 1998; St. Laurent & Garrett 2002; Kunze & Llewellyn Smith 2004; Wunsch & Ferrari 2004; Lamb 2014; Sarkar & Scotti 2017). Ocean observations have shown that although some of the waves are trapped in their generation sites and hence dissipate locally (Aucan *et al.* 2006; Carter & Gregg 2006; Lee *et al.* 2006; Levine & Boyd 2006; Klymak, Pinkel & Rainville 2008; Johnston *et al.* 2011; Nikurashin & Legg 2011), the majority of them can radiate to far away places (Ray & Mitchum 1996; Alford 2003; Alford & Zhao 2007; Nash *et al.* 2007; Kunze *et al.* 2012). These radiated waves will be largely dissipated when interacting with different kinds of ocean features such as continental slopes and seamounts (Eriksen 1982; Nash *et al.* 2004; Klymak *et al.* 2006; Zhao, Alford & Mackinnon 2010; Alford *et al.* 2011; Martini *et al.* 2011). To better understand the internal wave dissipation and its effects on the ocean mixing, many studies have been performed to simulate and determine quantitatively the wave–topography interactions, and one of the most studied cases is the reflection or scattering of incident internal waves upon the sloping topography.

When an internal wave beam propagates in a uniformly stratified fluid, the angle of its group velocity vector with respect to the horizontal, α , depends only on the wave frequency ω , if the effect of the Earth's rotation is neglected. The relation between α , ω and the buoyancy frequency N is given by (Sutherland 2010)

$$\tan \alpha = \sqrt{\frac{\omega^2}{N^2 - \omega^2}}. \quad (1.1)$$

Owing to such a property, an internal wave maintains its angle after scattering or reflection upon a slope, which can lead to much higher wavenumber and energy density, causing the instabilities and dissipation. Moreover, the overlap between the incident and reflected wave near the topography can also enhance significantly the nonlinear effects, which results in mean flow and harmonics. These physical phenomena can be influenced by several parameters, for example, the criticality (usually defined as the ratio of the topography slope to wave characteristic slope), the properties of the incident wave such as its amplitude, the shape or relative height of the topography, and the stratification of ambient fluid. Previous studies have explored thoroughly how the wave scattering depends on these control parameters (see e.g. Cacchione & Wunsch 1974; Thorpe & Haines 1987; Gilbert & Garrett 1989; Ivey & Nokes 1989; Taylor 1993; Ivey, Winters & De Silva 2000; Müller & Liu 2000*a,b*; Legg & Adcroft 2003; Gostiaux *et al.* 2006; Scotti 2011; Rodenborn *et al.* 2011; Chalamalla *et al.* 2013; Hall, Huthnance & Williams 2013; Legg 2014; Arthur, Koseff & Fringer 2017; Nazarian & Legg 2017*a,b*; Sarkar & Scotti 2017). However, the impact from another significant property, the roughness of the slope surface, has not been investigated systematically.

There are a number of previous studies that examine the role of surface roughness on wave scattering; all of them are theoretical. The first was by Longuet-Higgins (1969), who found that quite small-scale irregularities can completely alter the reflecting properties of a surface, and he also elucidated the impacts of different kinds of periodic surface roughnesses on wave transmission. A more quantitative study was shown by Mied & Dugan (1976), and they calculated the energy redistribution of the wave scattered by a sinusoidally corrugated surface. Thorpe (2001) was the first to use a configuration with

superimposed roughness elements on a sloping topography, and studied the scattering of an incident internal wave on such a topography. This work was further improved by Legg (2004), who incorporated the Coriolis effect. Later findings by Nakamura & Awaji (2009) indicate that the surface roughness can also change the frequency of the incident wave under some conditions. The above theoretical models have shed some light on the effects of surface roughness on wave scattering. However, there still exist some aspects that need to be explored, one of which is that the viscous effect was not incorporated in these models, and hence a major puzzle remains, i.e. how is the dissipation of wave energy affected by the surface roughness? The main purpose of the present work is to answer such a question through a laboratory study.

In this paper, we perform a laboratory experiment to investigate the scattering, energy dissipation and mean flow induced by the internal gravity wave incident upon slopes with different surface roughness. For completeness, we examine the role of criticality, while the impact from the amplitude of the incident wave is also illustrated. The remainder of this paper is organized as follows. The experimental apparatus with a novel design, the measurement techniques and the parameter space are introduced in § 2. The main results and discussions are shown in § 3, which is divided into four subsections. The structure of the generated wave in our system is presented in § 3.1. The fields of kinetic energy and wave dissipation near the topography are shown in § 3.2. The profiles of the averaged dissipation rate and kinetic energy are presented in § 3.3. The mean flow field induced by the nonlinear effect is shown in § 3.4. We summarize our findings and conclude in § 4.

2. Experimental apparatus and methods

As shown in figure 1, the experiments were performed in a box of rectangular shape with length L , width W , and height H equal to $80 \times 20 \times 20$ (cm), respectively. The working fluid that fills the box is deionized and degassed water. The top and bottom plates of the box are made of copper, with their surfaces electroplated with nickel and then chromium, while the side wall of the box is constructed by four transparent Plexiglas plates of thickness 2 cm. The top plate is heated by eight embedded heaters, and the heating power is controlled by a high-stability power supply; the bottom plate is cooled by a regulated refrigerated recirculator. For more details on the design of these plates, we refer to Xia, Sun & Zhou (2003).

In this experiment, the top and bottom temperatures of the box were fixed at 32.5°C and 11.5°C , respectively, thus the working fluid is stably stratified, with the strength of stratification being controlled by the temperature difference across the box. The surrounding temperature, controlled by two high-performance air conditioners, was set equal to the mean temperature of the box, i.e. 22.0°C . Comparing with the traditional approach, in which saline water is used to make a stably stratified fluid layer by the two-tank method (Fortuin 1960), our method has three main advantages. First, the generated stratification may be closer to that in the ocean, since the temperature, rather than salinity, has the greatest effect on density change in the ocean (Webb 2019). Second, once the stable stratification is established, we can perform wave field measurements at any time without the need to reproduce the stratification. Third, as the stratification is determined solely by the temperature distribution, it can be measured easily by scanning the temperature profile with a thermistor attached to a movable rod. In this experiment, we scan the vertical temperature profile with a step size 5 mm. The equation that is used to convert the temperature of water T at different vertical positions to its density ρ is

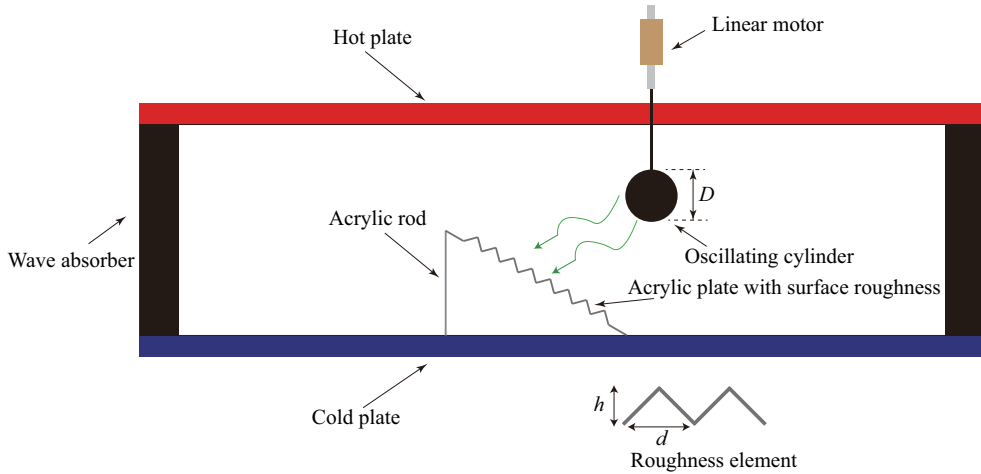


Figure 1. Schematic drawing of the experimental apparatus.

the Kell (1975) formulation

$$\rho = \frac{a_1 + a_2 T - a_3 \times 10^{-3} T^2 - a_4 \times 10^{-6} T^3 + a_5 \times 10^{-9} T^4 - a_6 \times 10^{-12} T^5}{1 + a_7 \times 10^{-3} T}, \quad (2.1)$$

where $a_1 = 999.83952$, $a_2 = 16.945176$, $a_3 = 7.9870401$, $a_4 = 46.170461$, $a_5 = 105.56302$, $a_6 = 280.54253$ and $a_7 = 16.897850$. The local buoyancy frequency is then obtained as

$$N(z) = \sqrt{-\frac{g}{\rho(z)} \frac{d\rho(z)}{dz}}, \quad (2.2)$$

where g is the gravitational acceleration, and z is the height relative to the bottom plate.

The quasi-two-dimensional internal gravity waves were generated by a smooth cylinder (19 cm in length and 5 cm in diameter), connected to a linear motor (model: P01-37 × 120/20 × 100-C, LinMot) that was set to oscillate periodically. The motion of the cylinder, which determines the dynamics of the generated internal wave, can be described by

$$Z(t) = A \cos(\omega t) + Z_0 - A, \quad (2.3)$$

where Z and Z_0 represent the vertical displacement and the initial vertical position of the generator relative to the bottom plate, while A and ω are the oscillating amplitude and frequency, respectively. A set of slopes was used in the experiment to model the sloping topographies in the oceans. Each of the slopes consists of a thin acrylic plate (19 cm in length, 19 cm in width, and 0.3 cm in thickness) with certain surface roughness, and two cylindrical acrylic rods (9.5 cm in height and 1 cm in diameter) that were used to support one end of the acrylic plate, with the other end resting on the bottom plate of the box. Such a design can minimize the influence of the added topographies on thermal stratification.

In the present study, the excited internal waves can propagate towards four directions. For simplicity, only the lower left wave beam, which interacts with the slope, is marked in figure 1 by two green wavy lines. The other three wave beams, undergoing one or several reflections at the top or bottom plates, will be absorbed by two foam filters (indicated by black rectangles in figure 1) with thickness 2 cm, which were placed at the left and right

ends of the tank. There is a vertical slit at the middle of the right foam filter so that the laser sheet can pass through.

The internal wave fields were measured by the particle image velocimetry (PIV) technique (Adrian 1991). The polyamide spheres ($20\ \mu\text{m}$ in diameter and $1.03\ \text{g cm}^{-3}$ in density) were selected as seeding particles. A continuous laser source (PSU-H-LED, MGL-H-532-400 mW) as well as some optics were used to produce a laser sheet to illuminate the seeding particles, and the flow field was recorded by a charge-coupled device (CCD) with 2048×2048 (pixel) resolution. The sampling rate was 2 Hz or 4 Hz, depending on the wave velocity, and the recording time is more than 40 wave periods for each measurement. The recorded raw images were processed by PIV calculation software (DPV-2010) to obtain two-dimensional velocity maps. For most of the measurements (except for that used to examine the generated wave structure), the number of grid points (the calculated vectors) within the region in which we are interested is about 120×60 , and the spatial resolution of the PIV measurement, i.e. the distance between the adjacent grids, is 1.7 mm. As the density of the seeding particles is slightly larger than that of the water (see figure 3a), it is necessary to test the impact from the sink of the particles on the measured flow field. We took a PIV measurement before the wave generator began to vibrate. The calculated velocities within the measuring window are almost zero, suggesting that this sedimentation effect can be neglected.

In this experiment, the buoyancy frequency within the measuring region is approximately $0.42\ \text{rad s}^{-1}$. The angle of each sloping topography with respect to the horizontal β is fixed at 30° , while the oscillating frequency ω , the oscillating amplitude A , and the wavelength of surface roughness, or simply surface roughness, λ on a slope, are variables. Here, λ is defined as the ratio of the height of the roughness element h to the width of its base d ($\lambda = h/d$, see figure 1), and h is fixed at 1 cm while d is varied, resulting in λ varying from 0.25 to 1.5. For comparison, we also conducted measurements using a slope with a smooth surface ($\lambda = 0$). The rough surface designed in this study is significantly different from that in a classical theoretical study mentioned above (Thorpe 2001). One of the main differences is that in Thorpe's case, the steepness of roughness relative to the slope, S , is supposed to be a small value ($S \ll 1$). Here, $S = 0.5hk$, with k being the wavenumber of the roughness element ($k = 2\pi/d$). In the current study, the calculated S varies from 0.79 to 4.71, which is close to or larger than 1. Such a difference makes the study in Thorpe (2001) less relevant to our experiment. The wave frequency ω in the present study is varied from 0.21 to $0.32\ \text{rad s}^{-1}$, so the angle of the generated incident waves with respect to the horizontal, α , which is calculated by (1.1), varied from 30° to 50° . In this study, there are two kinds of criticality. One of them is the criticality of large slope, which is usually defined as $\tan(\beta)/\tan(\alpha)$. To highlight the deviation from α to β , a new control parameter γ , the off-criticality, is introduced, defined as $(\alpha - \beta)/\beta$, and varies from 0 to 0.67 (such a definition is close to that in Chalamalla *et al.* 2013). Note that $\gamma = 0$ corresponds to a critical slope, and all non-zero positive values of γ correspond to subcritical slopes. We now turn to another kind of criticality, which is the criticality of a roughness element. Figure 2 shows a geometrical sketch of the internal waves incident on a roughness element. Here, we denote the angle between the right side of the roughness element and the horizontal as β_2 , which equals $\varphi + \beta$, where φ is the angle between the right side of the roughness element and the slope surface. The criticality of the roughness elements is usually defined as $\tan(\beta_2)/\tan(\alpha)$, which then equals $\tan(\alpha + \beta)/\tan(\alpha)$. Note that $\varphi = \arctan(2\lambda)$ (where λ is the surface roughness and equals h/d) and $\alpha = \gamma\beta + \beta$. The criticality of a roughness element can be expressed

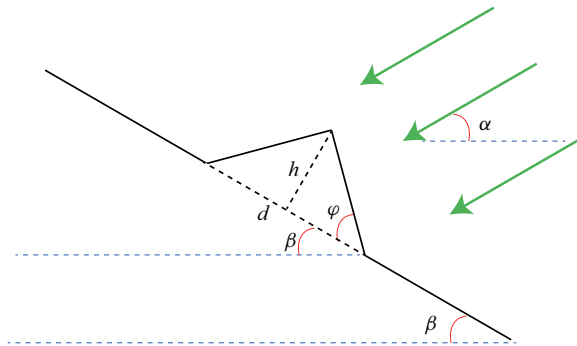


Figure 2. Illustration of internal waves incident on a roughness element. The green arrows represent the incident waves, and the solid black lines constitute a roughness element superimposed on a slope. Here, φ is the angle between the right side of the roughness element and the slope surface, α is the angle of the incident waves with respect to the horizontal, and β is the angle of the slope with respect to the horizontal. The width and height of the roughness element are denoted d and h , respectively. For simplicity, we plot only one of the roughness elements.

as $\tan(\arctan(2\lambda) + \beta) / \tan(\gamma\beta + \beta)$. Since β is fixed at 30° , we see that the criticality of a roughness element can be determined by λ and γ , and hence is not a new independent control parameter for our system. In Appendix C, we will show that the criticality of a roughness element is not a good choice as control parameter.

The amplitude A is set from 1.5 to 6 mm. Therefore, A/D varied from 0.03 to 0.12, where D is the diameter of the oscillating cylinder as indicated in figure 1. As the role of the wave amplitude in wave–topography interaction is not the main focus of this study, details of dependence of the scattered wave properties on the amplitude A will be illustrated in Appendix B.

3. Results and discussion

3.1. The generated wave beam in the absence of topographies

To begin with, we check the vertical density profile measured in the system, which is shown in figure 3(a). Here, the inset shows the measured temperature profile, which is used to calculate the density profile by (2.1). The buoyancy frequency N (calculated by (2.2)) is shown in figure 3(b), where there are four data sets that were measured over a period of one month. The overlap of these four data sets shows excellent stability of the established stratification. The buoyancy frequency is not uniform in the vertical direction. However, within the measuring region, indicated by the two dashed lines in figure 3(b), the buoyancy frequency is nearly constant, with mean value 0.42. As indicated by (1.1), the value of N determines the upper limit of the frequency of the generated wave.

We now examine the structure of the generated wave in our system in the absence of topographies. An example of the vector maps of the measured internal wave field is plotted in figure 4(a). Here, $A/D = 0.03$ and $\omega/N = 0.21$. Also, T is the length of the wave period, and $t = T/4$ is the time when the cylinder reaches the equilibrium position and moves downwards.

Assuming that the boundary condition at the surface of the wave generator is free-slip, and that the variation of the excited internal wave in the across-beam direction is much larger than that in the along-beam direction, Hurley & Keady (1997) proposed a viscous linear theory to describe the internal waves generated by a vibrating elliptic cylinder in

Internal gravity waves incident upon rough slopes

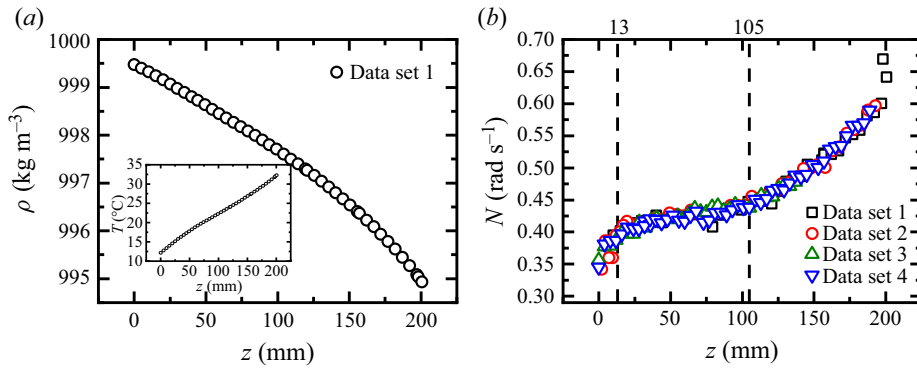


Figure 3. (a) The density profile from data set 1, which is calculated by the measured temperature profile (inset). (b) The profiles of buoyancy frequency from four data sets measured over a period of one month. The dashed lines indicate the vertical range of the measuring window.

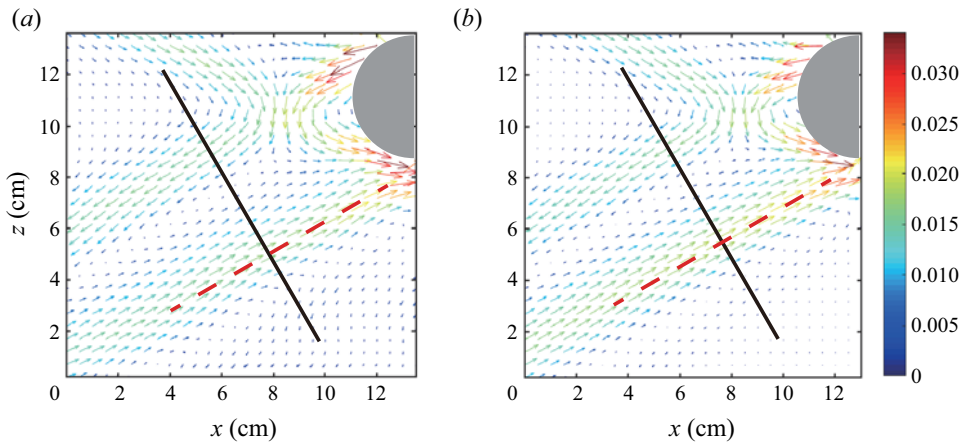


Figure 4. Vector maps of internal wave velocity with magnitude $\sqrt{u^2 + v^2}$ cm s⁻¹ coded in both colour and arrow length at $A/D = 0.03$, $\omega/N = 0.21$ and $t = T/4$: (a) experimental measurement; (b) theoretical prediction. The black solid line and red dashed line indicate, respectively, the perpendicular and parallel directions of the energy propagation of the waves.

stratified fluid of constant buoyancy frequency. Such a theory (referred to as HK theory hereafter) has been used to compare with previous experiments (Sutherland *et al.* 1999; Zhang, King & Swinney 2007). In figure 4(b), we plot the wave field predicted by the HK theory with the same values of the parameters as in the experiment. One sees that the experimentally measured wave field shows good correspondence with that predicted by theory.

To make a more quantitative comparison, we plot the profiles of along-beam velocity (velocity in the direction of wave propagation) V_a in figure 5, which are taken across the black lines shown in figure 4. Here, b represents the relative distance of the points on the black line to the centre of the line, and the minus or plus sign of b means the point is located below or above the midpoint on the black line. From figures 5(a) and 5(c), we see that the experimental results can be described very well by the HK theory. In figures 5(b) and 5(d), where the wave frequency becomes larger, it can be seen that HK theory under-predicts the wave amplitude when b is positive. The increase of the deviations between the experiments

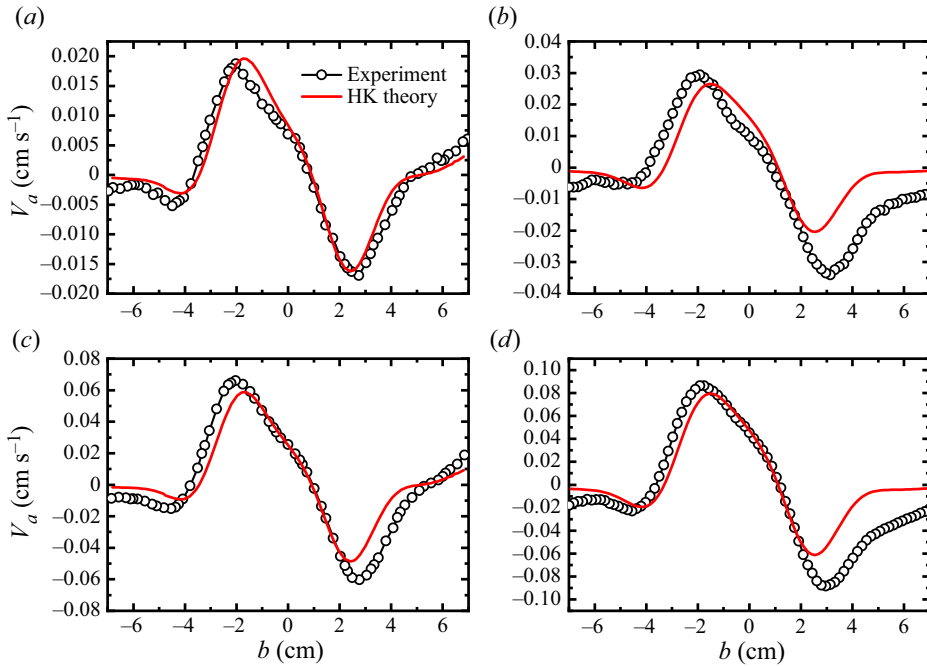


Figure 5. The profiles of along-beam velocity when $t = T/4$: (a) $A/D = 0.03$, $\omega/N = 0.21$; (b) $A/D = 0.03$, $\omega/N = 0.30$; (c) $A/D = 0.09$, $\omega/N = 0.21$; (d) $A/D = 0.09$, $\omega/N = 0.30$.

and the HK theory when ω increases was also found in Sutherland *et al.* (1999). This will not be discussed further as it is not the main focus in the present study.

Figure 6 shows the variation of the wave amplitude in the direction of the group velocity from our measurement and the prediction from the linear HK theory in a semi-logarithmic plot. One can see clearly that neither the experimental data nor the model prediction follows the exponential decay described by the classical wave attenuation equation for a monochromatic wave (Lighthill 1978). The figure also shows some differences between the experimental data and linear model prediction; the difference is about 10% in the largest case. Such a deviation is also found in some previous works. For example, in Zhang *et al.* (2007), the difference between the theory and experimental data can be as large as 50% (figure 6(d) in their paper).

3.2. Wave field near the rough slope

We now place the topography into the box and study the wave fields near the slopes with different surface roughness. The scattering of the incident internal waves can be seen clearly in figure 7, where we show the contour maps for the fields of time-averaged kinetic energy:

$$E = \frac{1}{t_2 - t_1} \int_{t_1}^{t_2} (u^2/2 + w^2/2) dt. \tag{3.1}$$

Here, u and w are the horizontal and vertical velocities, respectively, t_1 is a time when the flow reaches steady state, and t_2 is chosen such that $t_2 - t_1$ is larger than at least 30 oscillating periods. For simplicity, we show only the results when $A/D = 0.03$ and $\gamma = 0.50$. Figures 7(a) to 7(e) show that the internal waves are modulated by the

Internal gravity waves incident upon rough slopes

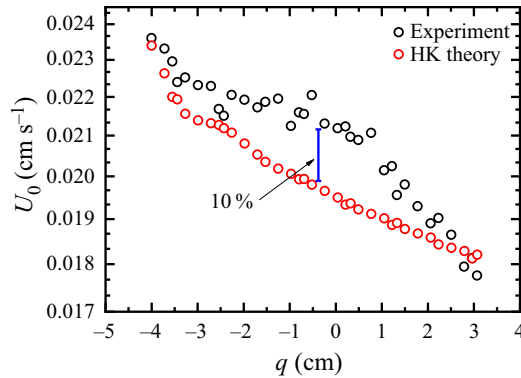


Figure 6. The variation of wave amplitude in the direction of the group velocity. The data are taken at the positions indicated by the red dashed lines in figure 4. q is the coordinate along the direction of the group velocity of the waves. The origin of q is the cross point of black solid lines and red dashed lines in figure 4. Note that the vertical scale in this figure is logarithmic.

surface roughness of the slope: The wave patterns exhibit light and dark stripes in the whole flow field. This is because of the constructive/destructive interference between the incident waves and the reflected waves. This effect becomes increasingly prominent as the roughness parameter λ is increased from 0 to 0.5. As λ becomes larger than 0.5, and the wavelength of the roughness becomes small, this kind of modulation is weakened. When $\lambda = 1.5$, the wave field is very close to that in smooth surface case. One may also find that high-intensity regions of the wave are around the peak positions of the roughness elements, which is due to the energy concentration during the wave reflection. Low-intensity regions correspond to the valley positions of the roughness elements, because part of the wave is trapped near the valley and hence becomes stagnant. Moreover, figure 7 shows that the kinetic energy of an internal wave is the largest in the region very close to the surface of the topography. Surprisingly, this maximum value shows no significant dependence on λ .

In figure 8, we show the fields of time-averaged dissipation rate:

$$\epsilon = \frac{1}{t_2 - t_1} \int_{t_1}^{t_2} \epsilon \, dt, \quad (3.2)$$

where ϵ is the instantaneous dissipation rate of kinetic energy in two-dimensional flow (Pope 2000):

$$\epsilon = \nu \left[2 \left(\frac{\partial u}{\partial x} \right)^2 + 2 \left(\frac{\partial w}{\partial z} \right)^2 + \left(\frac{\partial u}{\partial z} + \frac{\partial w}{\partial x} \right)^2 \right]. \quad (3.3)$$

Here, ν is the kinematic viscosity of water. To measure the dissipation rate accurately, the Kolmogorov length scale should be resolved in the PIV measurement. However, the spatial resolution should not be too high, otherwise the measurement error increases (Tokgoz *et al.* 2012). In this experiment, it is difficult to realize fully the above requirements at each grid point because of the spatial inhomogeneity, i.e. the resolution is a bit too low for some high-dissipation region, but may be a little too high for some low-dissipation region. Hence a direct comparison between the measured dissipation field in the rough surface cases and that in the smooth surface case can be only qualitative.

Figures 8(a) to 8(e) show the modulation of the surface roughness on the energy dissipation of internal waves. For all cases, the energy dissipation is the largest near the

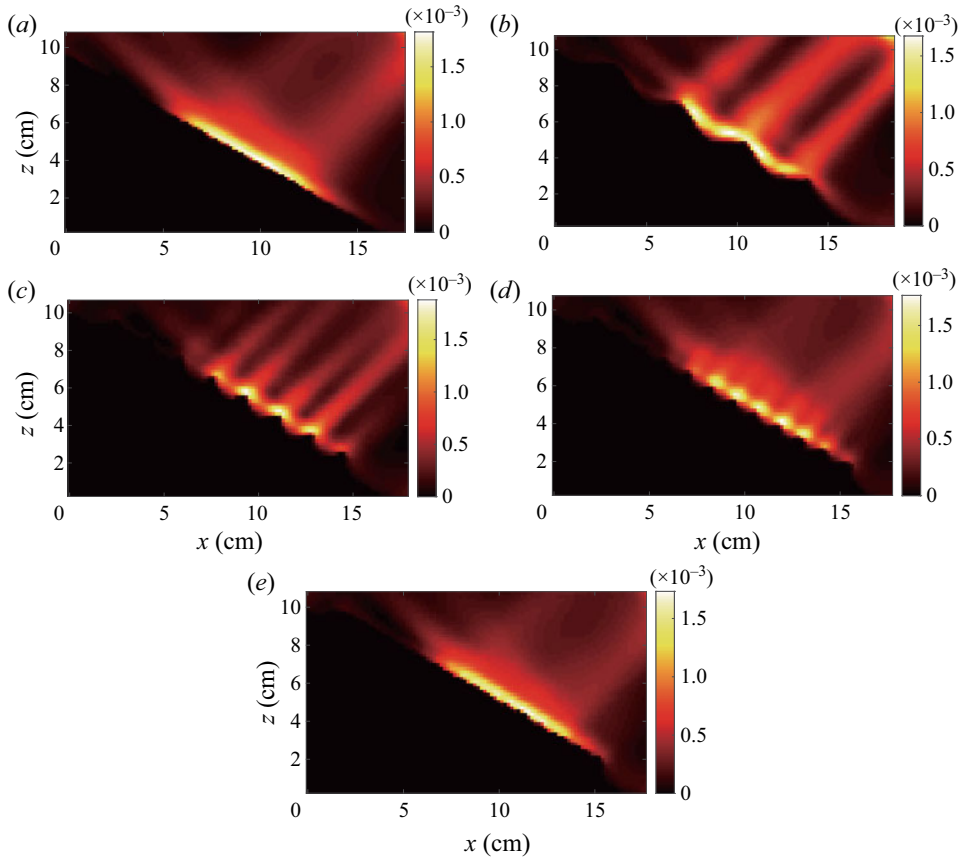


Figure 7. Contour maps for the fields of time-averaged kinetic energy at different λ when $A/D = 0.03$ and $\gamma = 0.50$: (a) $\lambda = 0$, (b) $\lambda = 0.25$, (c) $\lambda = 0.5$, (d) $\lambda = 0.75$, (e) $\lambda = 1.5$. The units are $\text{cm}^2 \text{s}^{-2}$.

slope, and the maximum energy dissipation in the smooth surface case is even larger than that in the rough surface case. On the other hand, in the roughness case, the region of intense dissipation seems to be less localized and is extended beyond the vicinity of the surface. This results in the distribution of dissipation rate in the rough cases being more uniform in space. Again, the dissipation field at $\lambda = 1.5$ is found to be close to that in the smooth surface case.

3.3. Profiles of dissipation rate and kinetic energy

To analyse quantitatively the effect of roughness on internal wave field, we plot and then examine the profiles of the averaged dissipation rate along the direction normal to the slope. We first introduce a new coordinate system shown in figure 8(b): the origin is set at halfway along the slope surface. Two variables, s and σ , represent the coordinates parallel and perpendicular to the slope surface, respectively. We then take the average of ϵ in the s direction:

$$\langle \epsilon \rangle(\sigma) = \frac{1}{\Delta} \int_{s_1}^{s_2} \epsilon(\sigma, s) ds, \tag{3.4}$$

Internal gravity waves incident upon rough slopes

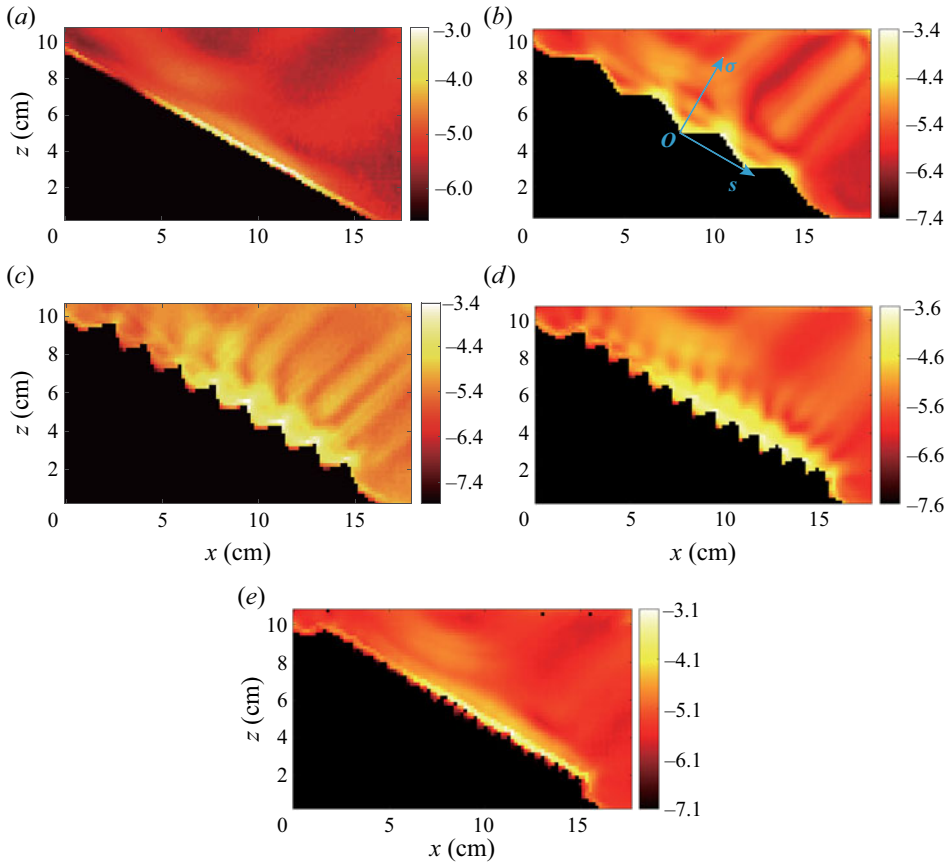


Figure 8. Contour maps for energy dissipation at different λ when $A/D = 0.03$ and $\gamma = 0.50$: (a) $\lambda = 0$, (b) $\lambda = 0.25$, (c) $\lambda = 0.5$, (d) $\lambda = 0.75$, (e) $\lambda = 1.5$. The value of $\log_{10}\langle\epsilon\rangle_t$ is coded in colour. The units are $\text{cm}^2 \text{s}^{-3}$.

where s_1 and s_2 are equal or close to $-l/2$ and $l/2$, respectively, in the region near the slope, l being the length of the rough surface of the slope ($l = 16 \text{ cm}$). Also, $\Delta = (s_2 - s_1)\xi$, where ξ is the ratio of the number of the grid points outside the roughness elements to the total number of grid points at a certain σ . In the region far away from the slope, the length of the average region, i.e. $s_2 - s_1$, would be smaller than l due to the finite size of the measuring window, which may partly reduce the accuracy of $\langle\epsilon\rangle$. However, as most of the energy is dissipated near the slope, such a finite size effect is negligibly small in the final results. Although the measured energy dissipation may be less than accurate at some grid points, as mentioned before, we have verified that the obtained profiles of $\langle\epsilon\rangle$ are accurate and reliable (for details about the verification, please refer to [Appendix A](#)). For simplicity, we will show only the dissipation profiles that were measured with $A/D = 0.03$.

In [figures 9\(a,b\)](#), we plot the normalized average dissipation rate $\langle\epsilon\rangle/\epsilon_0$ versus the normalized distance normal to the slope, σ/h . Here, $\epsilon_0 = A^2\omega^3$, and h is the height of the roughness element, as we said before. These figures show that the surface roughness reduces the maximum value in the dissipation profile. It is also seen that the peak width of the profiles in the rough cases is larger than that in the smooth surface case. This is consistent with the observation from [figure 8](#) that the energy dissipation becomes less

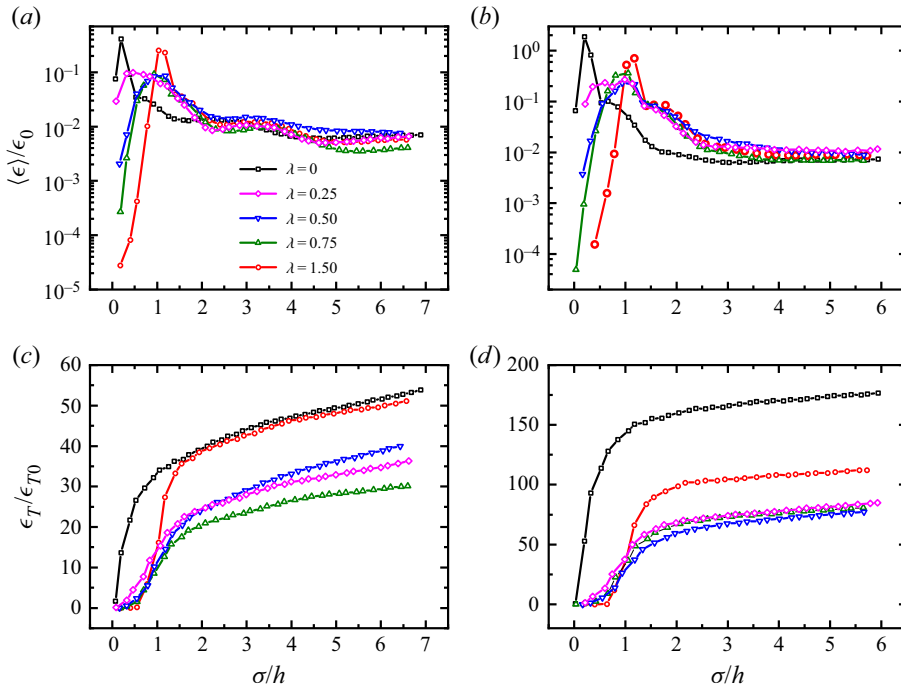


Figure 9. Profiles of (a,b) the along-slope and time-averaged dissipation rates, and (c,d) the accumulated dissipation rate. For (a,c) $\gamma = 0.5$, and for (b,d) $\gamma = 0.17$. Different symbols represent different roughnesses as shown in (a).

localized and is spatially more uniform when the slope surface is rough. Another feature shown in these figures is that when $\lambda \geq 0.50$, the energy dissipation is very weak when σ is very close to the valley of the roughness ($\sigma \approx 0$). A possible reason is that part of the incident wave is trapped near the valley of the roughness elements and hence become stagnant, as we said before. The results are the same for other values of γ . In figures 9(c,d), we plot the profiles of the normalized accumulated dissipation rate, $\epsilon_T / \epsilon_{T0}$. Here, ϵ_T is defined as

$$\epsilon_T(\sigma) = \frac{\rho W_0 l}{s_2 - s_1} \int_0^\sigma \int_{s_1}^{s_2} \epsilon(\sigma, s) ds d\sigma, \quad (3.5)$$

where ρ_0 is the density of water, and W_0 is the width of the slope. Also, $l/(s_2 - s_1)$ is the normalization factor, which is used to make the integral length in the s direction remain the same at different σ , and thus can reduce the impact from the finite size of the measuring window. As (3.5) shows, $\epsilon_T(\sigma)$ reflects the total amount of energy dissipation in the region below a certain σ . We have $\epsilon_{T0} = \rho_0 l_0^3 A^2 \omega^3$, where l_0 is the unit length (1 cm). Both figures 9(c) and 9(d) show that the surface roughness can also reduce the total amount of the energy dissipation, and this roughness-induced reduction shows a clear dependence on λ . When comparing figures 9(c) with 9(d), we see that the roughness-induced reduction is much more prominent at $\gamma = 0.17$, suggesting that such a reduction is also highly related to the off-criticality.

In figure 10, we examine the influence of the off-criticality on the energy dissipation, where the profiles of the averaged and accumulated dissipation rates are both shown for various values of γ . It is found that there exists a non-zero optimal off-criticality

Internal gravity waves incident upon rough slopes

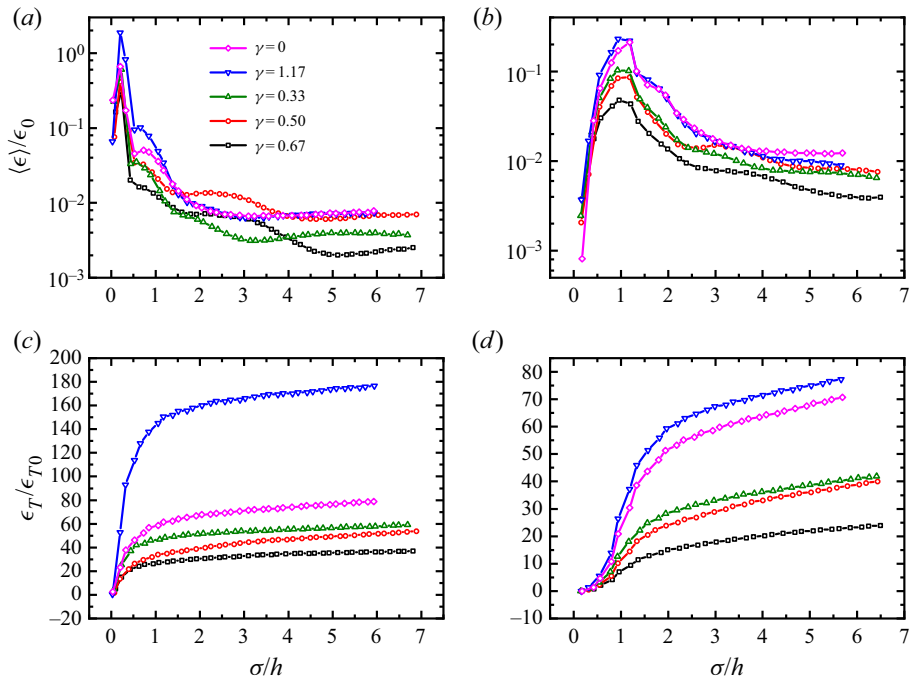


Figure 10. Profiles of (a,b) the normalized average dissipation rate, and (c,d) the accumulated dissipation rate. For (a,c) $\lambda = 0$, and for (b,d) $\lambda = 0.5$. Different symbols represent different off-criticality.

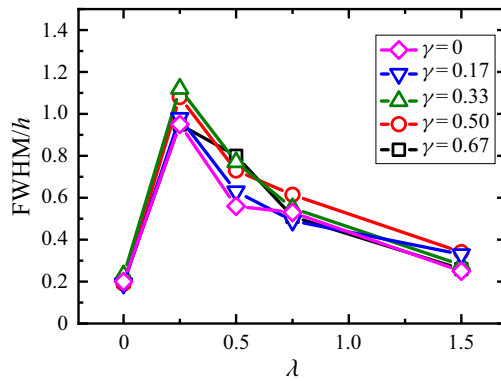


Figure 11. Full width at half-maximum (FWHM) of the profiles of the averaged dissipation rate versus λ at different γ .

($\gamma_{optimal} = 0.17$) for energy dissipation in both the smooth and rough surface cases. Surprisingly, unlike surface roughness, the off-criticality is found to apparently have no effect on the peak width of the dissipation profile, but affects its shape only far from the slope. This suggests a weak dependence of the spatial distribution of the dissipation on off-criticality, which is confirmed further in figure 11.

In figure 11, we plot the normalized full width at half-maximum (FWHM) of the peaks in the profiles of the averaged dissipation rate versus λ at different γ . It is seen that the peak width of the dissipation profile indeed depends weakly on off-criticality, as the

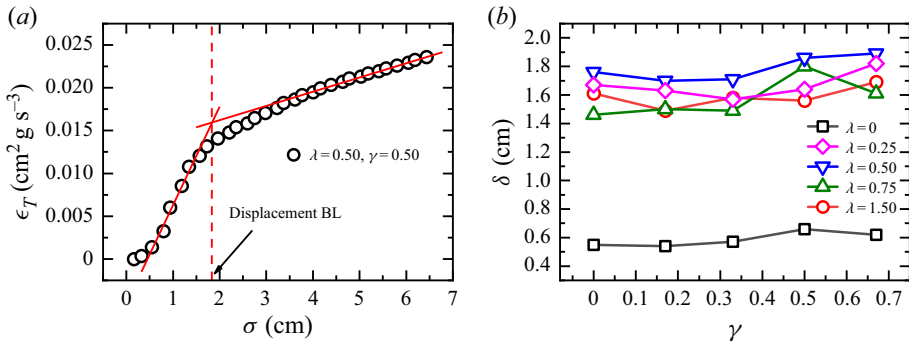


Figure 12. (a) Illustration of determining the thickness of the displacement boundary layer (DBL) by the slope method. (b) The thickness of the DBL versus off-criticality at different surface roughnesses.

values of $FWHM/h$ at different γ are close. Rather, $FWHM/h$ of the dissipation profiles is determined mainly by the surface roughness. The peak width in rough surface cases can be much larger than that in the smooth surface case, as figure 9 shows. Moreover, the peak width increases monotonically when λ decreases from 1.50 to 0.25. Figure 11 demonstrates quantitatively that the region of intense dissipation is broadened due to the effect of surface roughness.

From both figures 9 and 10, we see that the energy dissipation accumulates rapidly in the region near the slope (except for the regions where σ is very close to 0 in some rough surface cases, i.e. near the valley of the roughness elements), and then accumulates very slowly in the region far from the slope. We introduce a quantity called the displacement boundary layer (DBL), which is used to separate the rapid accumulation and slow accumulation regions. The method to determine the thickness of the DBL is shown in figure 12(a). We extrapolate the linear parts of the accumulated dissipation profile both near the slope and far from the slope, and the distance from the slope at which these two extrapolating lines cross corresponds to the thickness of the DBL. We plot the thickness of the DBL (δ) versus the off-criticality γ at different surface roughnesses λ in figure 12(b), which shows that δ has a weak dependence on γ , and the data scatter may be due to the errors in determining the DBL thickness. The figures also show that the DBL thickness for the smooth surface is much smaller than for the rough cases. The differences between the DBL thicknesses in the smooth and rough surface cases are close to the height of the roughness element. This suggests that such differences are determined mainly by the height of the roughness element.

To examine the effects of roughness on energy dissipation more completely, we plot in figure 13(a) the maximum value of the averaged dissipation $\langle \epsilon \rangle_{max}$ in the profiles measured at all γ , versus the surface roughness λ . It is seen that for each γ , $\langle \epsilon \rangle_{max}$ first decreases and then increases with increasing λ . Except for the case with $\gamma = 0$, $\langle \epsilon \rangle_{max}$ reaches a minimum at $\lambda = 0.5$, where the modulation effect is most pronounced, as shown in figure 7. The ratio of $\langle \epsilon \rangle_{max}$ at $\lambda = 0$ (smooth surface case) to that at $\lambda = 0.5$ can be as large as ~ 10 . We also plot the total dissipation rate at $\sigma = 2\delta$, namely $\epsilon_T|_{\sigma=2\delta}$, versus λ in figure 13(c). When σ reaches 2δ , the dissipation has decayed significantly and the accumulated dissipation ϵ_T increases very slowly with the distance σ , hence $\epsilon_T|_{\sigma=2\delta}$ can be used as a measure of the total energy dissipation. Although the relation between $\epsilon_T|_{\sigma=2\delta}$ and λ is somewhat complex, a broad feature is that the surface roughness reduces $\epsilon_T|_{\sigma=2\delta}$ under most circumstances. Figure 13(c) also shows that the total energy dissipation has

Internal gravity waves incident upon rough slopes

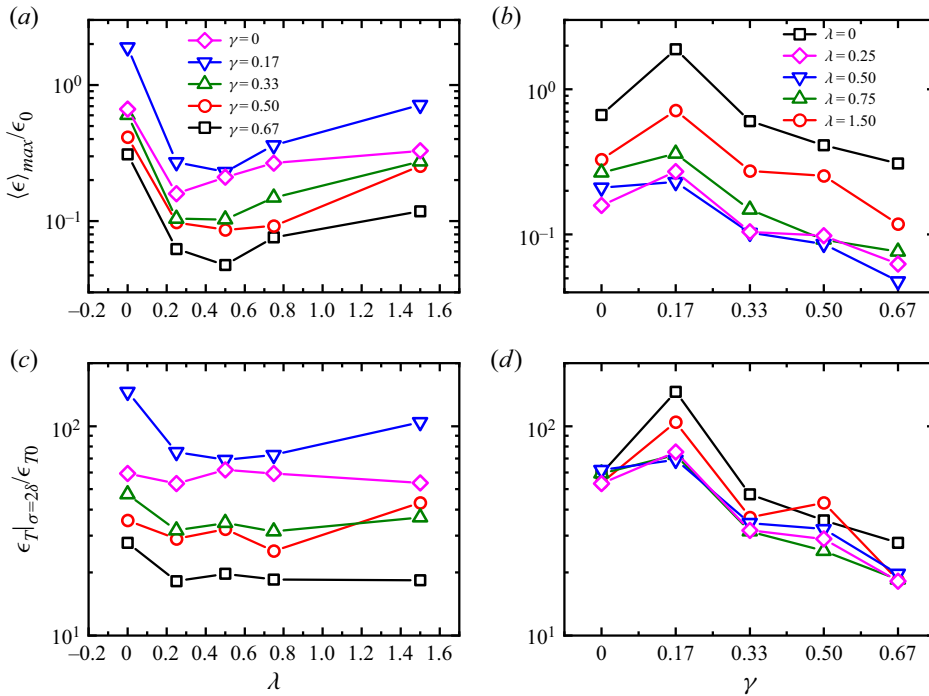


Figure 13. Maximum value in the averaged dissipation profile $\langle \epsilon \rangle_{max} / \epsilon_0$ versus (a) roughness λ , and (b) off-criticality γ . Accumulated dissipation rate at $\sigma = 2\delta$, $\epsilon_T |_{\sigma=2\delta} / \epsilon_{T0}$, versus (c) roughness λ , and (d) off-criticality γ . The symbols represent different off-criticality in (a,c), and different surface roughnesses in (b,d).

less dependence on λ when compared with the maximum value in the dissipation profile. The reason is that although the surface roughness reduces the maximum value of the dissipation rate, it broadens the region of intense dissipation. The combination of these two effects reduces the dependence of the total accumulated dissipation on the surface roughness. In figures 13(b) and 13(d), we plot $\langle \epsilon \rangle_{max}$ and $\epsilon_T |_{\sigma=2\delta}$ versus off-criticality γ , respectively. It is clear that there exist an optimal off-criticality at which both $\langle \epsilon \rangle_{max}$ and $\epsilon_T |_{\sigma=2\delta}$ reach their respective maximums. This optimum off-criticality remains invariant for different surface roughnesses, and equals 0.17. It should be noted that because of the sparsity of the data, this number serves to provide only a rough measure of the true optimal value. Another feature seen from figure 13(d) is that the value of $\epsilon_T |_{\sigma=2\delta}$ for $\gamma = 0$, i.e. waves with critical incidence, is the same for surfaces with different roughnesses, even for a smooth surface, which is somewhat unexpected. It would be interesting to explore the relation between the criticality of the slopes of the roughness elements (the definition of the criticality is shown in § 1) and the energy dissipation of waves. However, as already mentioned (see Appendix C for details), this criticality is not a good choice as a control parameter.

It is known that stronger flow strength usually leads to stronger energy dissipation. Thus we also investigate the relationship of wave energy to surface roughness and off-criticality. In figure 14, we plot the profiles of the normalized average kinetic energy $\langle E \rangle / E_0$. Here, the method to obtain the time- and space-averaged kinetic energy $\langle E \rangle$ is the same as that used to obtain $\langle \epsilon \rangle$ in (3.4), and E_0 used for the normalization equals $A^2 w^2$. From figures 14(a) and 14(b), we see that the surface roughness has little effect on the strength

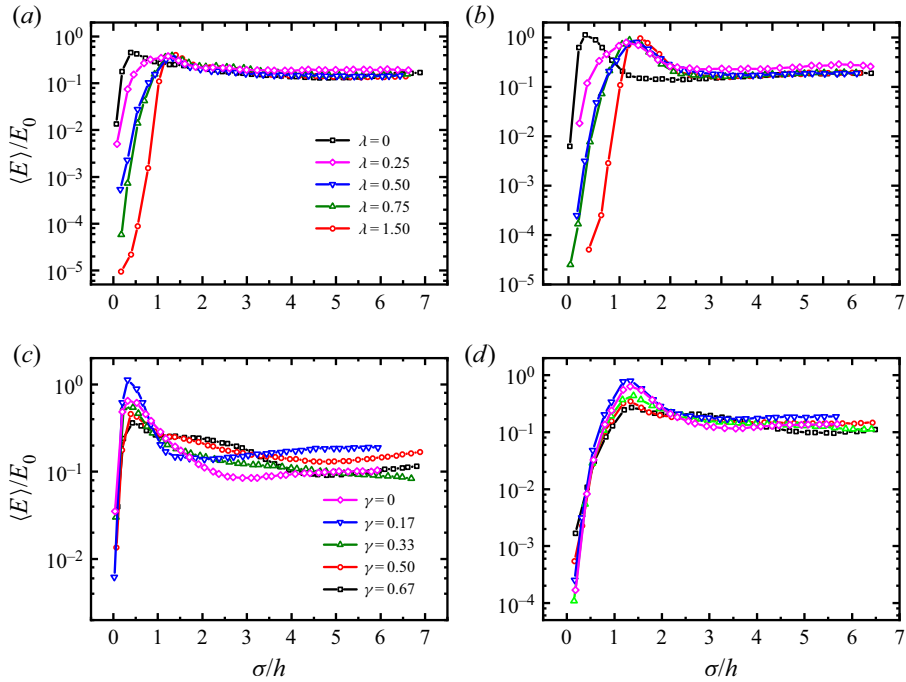


Figure 14. Profiles of the normalized averaged kinetic energy $\langle E \rangle / E_0$ at different surface roughnesses λ , with (a) $\gamma = 0.5$, and (b) $\gamma = 0.17$; and at different off-criticality γ , with (c) $\lambda = 0$, and (d) $\lambda = 0.5$.

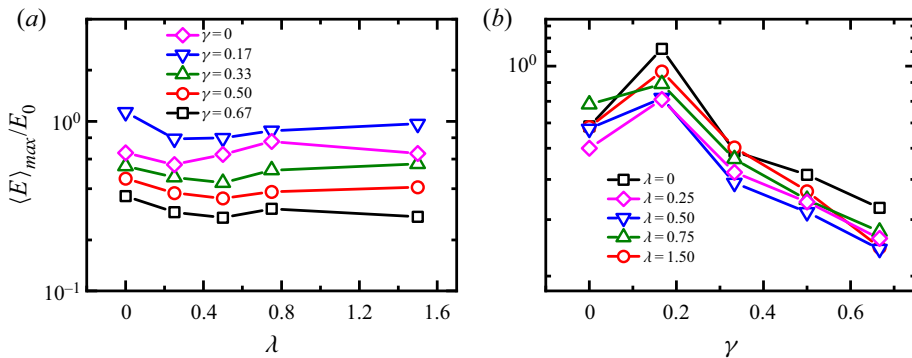


Figure 15. Maximum value in the averaged kinetic energy profile $\langle E \rangle / E_0$ versus (a) roughness, and (b) off-criticality.

of the internal wave near the slope except that it shifts the peak position position by a distance roughly equal to the height h of the roughness elements (1 cm). Figures 14(c) and 14(d) show that the wave energy near the slope can be affected by off-criticality. The more quantitative examination is shown in figure 15, where we plot the maximum value in the profile of averaged wave energy $\langle E \rangle_{max} / E_0$ versus surface roughness λ in (figure 15a) and vs off-criticality λ in (figure 15b). Indeed, the wave energy near the slope has no significant dependence on surface roughness, but is dependent only on the off-criticality. The optimum γ equals 0.17 and is the same as that found in figures 13(b) and 13(d).

In some of the previous studies, critical reflection ($\gamma = 0$) has attracted most of the attention as it can result in the strongest wave energy near the slope according to the linear inviscid theory. However, the present study suggests that the strongest wave energy exists at off-criticality 0.17, not 0. In our understanding, the optimum off-criticality should be determined by two effects: the energy concentration effect, which enhances the wave energy near the slope, and the effect induced by the bottom drag, which reduces the wave energy. When the off-criticality decreases to zero, both of these effects are enhanced continuously, and their combination leads to a non-zero optimum off-criticality. In the classical theory, the viscous effect is not incorporated, hence the optimum off-criticality should be zero. The existence of non-zero optimal off-criticality is also found in other studies; e.g. Chalamalla *et al.* (2013) reported that the turbulent kinetic energy can be higher for somewhat off-critical reflection compared to exactly critical reflection under certain conditions. A weakly nonlinear model (Kataoka & Akylas 2020) also shows that in some conditions, the viscous effect can be important during the wave reflection from a slope, which leads to the deviation of the optimal off-criticality from zero.

3.4. Mean flow

As mentioned in § 1, the mean flow field induced by the interaction between incident wave and topography can reflect the strength of the nonlinear effect. The previous theoretical and experimental studies have elucidated clearly the two-dimensional mean flow field near slopes with smooth surface (Thorpe & Haines 1987; Grisouard 2010). In this subsection, we focus on the influence of surface roughness on the mean flow field. The vector map of the mean flow velocity $U\mathbf{e}_x + W\mathbf{e}_z$ for the smooth surface and rough surface cases are shown in figures 16(a) and 16(b), respectively. Here, U and W are long-time-averaged horizontal and vertical velocities, while \mathbf{e}_x and \mathbf{e}_z are the rightward and upward unit vectors, respectively. A comparison between these two figures clearly shows that the surface roughness changed the structure of the mean flow field: a series of vortices, of size roughly the same as the separation between the tips of roughness elements, are formed near the slope surface. In the case of a smooth surface, the direction of the mean flow is mainly parallel to the slope. However, in the rough surface case, the formation of vortices is accompanied by the enhancement of mean flow in the direction perpendicular to the slope, which is further confirmed in figures 16(c) and 16(d), where we show the contour plots of mean flow velocity in the direction perpendicular to slope surface V_σ . It is found that V_σ in the rough surface case is much stronger than that in the smooth surface case (notice the difference in the scale bar). For comparison, we also plot the fields of the mean flow velocity in the direction parallel to slope V_s in figures 16(e) and 16(f). Although the roughness elements would induce additional bottom drag force as we mentioned before, it is found that the strength of V_s in the rough surface case is even slightly larger than that in the smooth surface case.

The normalized maximum values of mean flow velocity in the direction normal to slope $(V_\sigma/V_0)_{max}$ versus surface roughness λ and off-criticality γ are plotted in figures 17(a) and 17(b), respectively. Here, $V_0 = A\omega$ is used for normalization. It can be seen that $(V_\sigma/V_0)_{max}$ first increases and then decreases as λ increases continuously. Interestingly, the maximum value of $(V_\sigma/V_0)_{max}$, which represents the strongest nonlinear effect, corresponds to the position $\lambda = 0.5$, at which the scattering effect becomes strongest, as shown in figure 7, and $\langle \epsilon \rangle_{max}$ reaches a minimum. From figure 17(b), it is found that

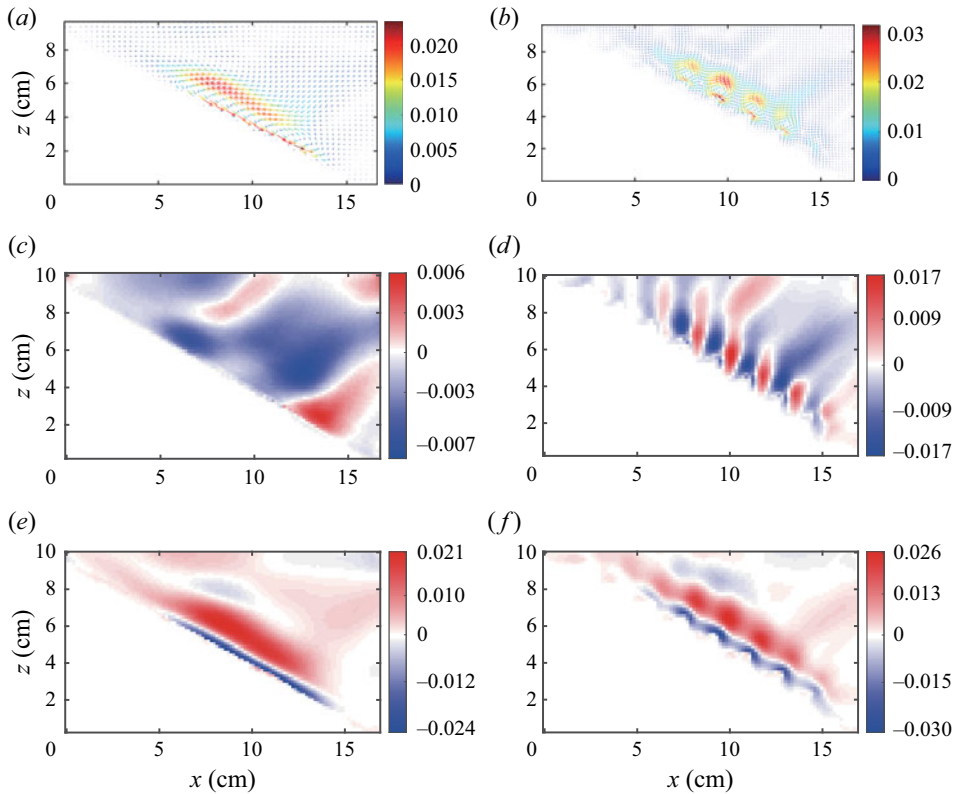


Figure 16. (a,b) Coarse-grained vector maps of the mean flow velocity $Ue_x + Ve_z$, with the magnitude $\sqrt{U^2 + W^2}$ coded in both colour and arrow length for the smooth and rough cases, respectively. (c,d) Colour-coded contour plots of mean flow velocity in the direction parallel to slope V_s . (e,f) Colour-coded contour plots of the mean flow velocity perpendicular to slope V_σ . In (a,c,e) $\lambda = 0$; in (b,d,f) $\lambda = 0.5$. Here, $A/D = 0.09$, $\gamma = 0.50$, and the units are cm s^{-1} .

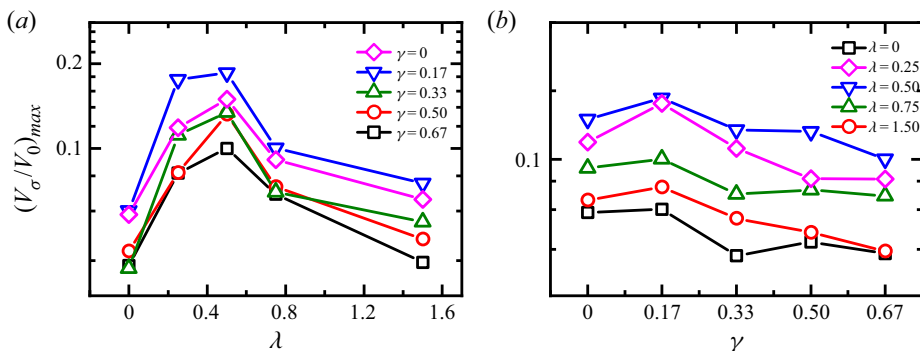


Figure 17. Normalized maximum value of the mean flow velocity perpendicular to slope, $(V_\sigma/V_0)_{max}$, versus (a) roughness λ , and (b) off-criticality $(\alpha - \beta)/\beta$.

there also exists an optimal off-criticality ($\gamma = 0.17$) for $(V_\sigma/V_0)_{max}$. The existence of an optimal off-criticality for mean flow is not difficult to understand, as the wave energy near the slope is largest at that off-criticality, as shown in figure 15(b).

4. Conclusion

In this paper, we have investigated experimentally the scattering, energy dissipation and mean flow when the incident internal waves are scattered by sloping topographies with rough surfaces in a stably stratified fluid maintained by a constant temperature gradient. The surface roughness λ (the ratio of the height of the roughness element to the width of its base) and the off-criticality γ (which relates directly to the wave frequency) are chosen as two main variables of the experiment, while the wave amplitude A is fixed in most cases.

As a validity check of the design of our system, the quality of the generated internal wave, and the measurement techniques, we first examine the generated wave beams in the absence of the topographies in the fluid. When comparing the obtained results with a viscous linear theory developed by Hurley & Keady (1997), which is a widely used linear model, it is found that the structure of the internal wave in our system can be well described by this theory. The scattering of incident wave by the surface roughness is shown in both the time-averaged kinetic energy field and the energy dissipation field. The effect of scattering enhances as λ increases from 0 to 0.5, and then weakens as λ increase from 0.5 to 1.5. Moreover, the distribution of energy dissipation is found to be more uniform in the direction perpendicular to the slope when the slope surface is rough. Counter-intuitively, although the roughness elements should enhance the drag force on the surface of the slope, both the maximum value in the profile of space- and time-averaged energy dissipation, $\langle \epsilon \rangle_{max}$, and the total energy dissipation, $\epsilon_T|_{\sigma=2\delta}$, are reduced by the surface roughness under most circumstances. Nevertheless, the peak width of the dissipation profile is found to be broadened significantly in the rough surface cases, which demonstrates that the intense dissipation region can be extended by the surface roughness. The peak width is found to increase monotonically when λ decreases from 1.50 to 0.25. Interestingly, the roughness is also found to affect strongly the mean flow field induced by wave-topography interaction. The structure of mean flow has been changed drastically by roughness: a series of vortices, of size roughly the same as the separation between the tips of roughness elements, are formed near the slope. Contrary to its role in energy dissipation, the surface roughness greatly enhances the mean flow in the direction perpendicular to the slope surface. The normalized maximum value of mean flow velocity in the direction normal to the slope, $(V_\sigma/V_0)_{max}$, reaches its maximum at $\lambda = 0.5$, at which the scattering becomes strongest and $\langle \epsilon \rangle_{max}$ reaches minimum.

The role played by off-criticality γ is examined systematically. It is observed that there exists an optimal γ ($= 0.17$ for the present measurement resolution) for the normalized $\langle \epsilon \rangle_{max}$ and $\epsilon_T|_{\sigma=2\delta}$, which may be attributed to the strongest kinetic energy near the slope at that γ . The combination of energy concentration effect and the effect induced by bottom drag force should be responsible for the existence of this non-zero optimal off-criticality, which is different from the prediction of linear inviscid theory. Not surprisingly, the same optimal off-criticality is found in the measured mean flow field when λ is varied. Unlike surface roughness, the off-criticality has only a small effect on the distribution of energy dissipation.

Our study suggests, under the present conditions, that the surface roughness of topography can reduce both the maximum energy dissipation and total energy dissipation. Furthermore, the surface roughness is found to broaden the region of intense dissipation. The wave-induced mean flow is also enhanced by the surface roughness. Moreover, there exists a non-zero optimal off-criticality at which the dissipation near the topography reaches maximum. In the oceans, topographies with rough surfaces are thought to be the regions where energy dissipates strongly (see e.g. Ledwell *et al.* 2000). The present study therefore provides a new perspective on how the surface roughness on

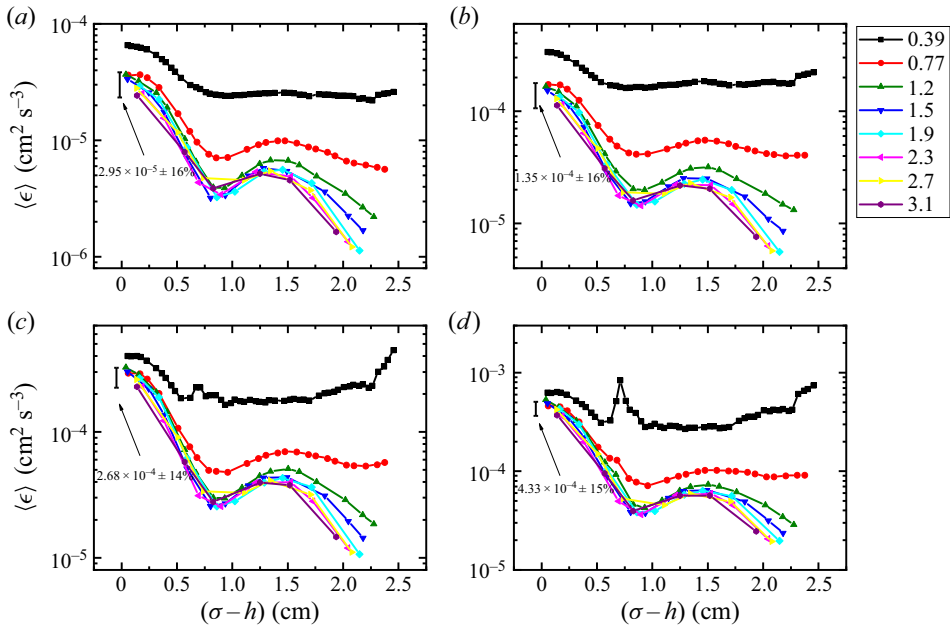


Figure 18. The profiles of time and along-slope averaged dissipation rate $\langle \epsilon \rangle$ measured at different resolutions when $\lambda = 0.25$ and $\gamma = 0.5$: (a) $A/D = 0.03$, (b) $A/D = 0.06$, (c) $A/D = 0.09$, and (d) $A/D = 0.12$. Different symbols represent different resolutions, the values of which are listed to the right of (b) with the unit mm. The values and errors of $\langle \epsilon \rangle$ at $\sigma = h$ are also given.

topographic features influences energy dissipation. Finally, we remark that further studies are needed to examine whether the present laboratory findings can be extended to the oceans.

Acknowledgements. The authors would like to thank S.-D. Huang for his help in the design of the experimental setup and for stimulating discussions, and thank G.-Y. Ding for technical assistance.

Funding. We gratefully acknowledge support of this work by the National Natural Science Foundation of China (grant no. 12072144), the Research Grants Council (RGC) of HKSAR (grant nos CUHK14301115 and CUHK14302317) and the Department of Science and Technology of Guangdong Province (grant no. 2019B21203001).

Declaration of interests. The authors report no conflict of interest.

Author ORCIDs.

Ke-Qing Xia <https://orcid.org/0000-0001-5093-9014>.

Author contributions. Y.-H.H. and B.-Y.-C.C. contributed equally to this work.

Appendix A. Test the reliability of the calculated dissipation profile

Here, we test the accuracy and reliability of the profile of the time and along-slope averaged energy dissipation $\langle \epsilon \rangle$ measured using the current spatial resolution. Figure 18 shows the profiles of the averaged dissipation measured at different resolutions (from 0.39 to 3.1 mm). For simplicity, λ is fixed at 0.25, while γ is fixed at 0.5. Note that to achieve high spatial resolution, the PIV measuring window in this test is limited to a small region near the slope, hence the measured dissipation profiles would be a little different from that shown in figure 9. From figures 18(a–d), it is found that all the profiles with

Internal gravity waves incident upon rough slopes

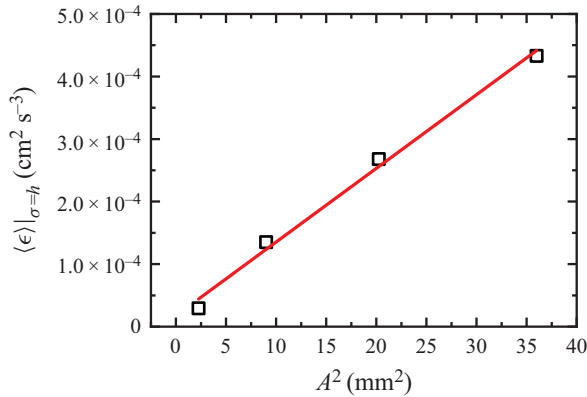


Figure 19. Plot of $\langle \epsilon \rangle$ at $\sigma = h$ versus A^2 when $\lambda = 0.25$ and $\gamma = 0.5$.

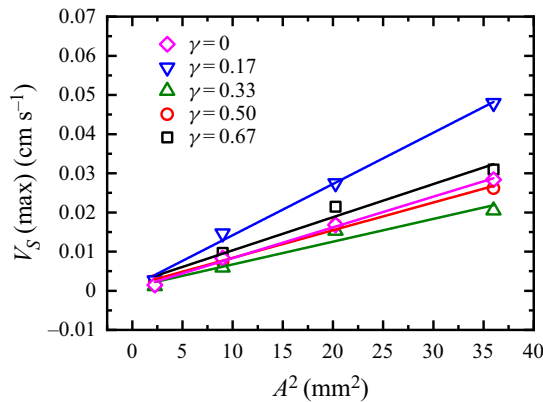


Figure 20. The maximum mean flow velocity in the direction parallel to the slope $V_s(\text{max})$ versus A^2 when $\lambda = 0$.

their measuring resolutions within the range from 1.5 mm to 3.1 mm can collapse nicely onto a single curve, which means that the resolutions within this range are appropriate for measuring the dissipation profiles. The chosen spatial resolution in the present PIV measurement is 1.7 mm, thus the profiles of $\langle \epsilon \rangle$ in this study are reliable. The values and the errors of $\langle \epsilon \rangle$ at $\sigma = h$, which are the mean and standard deviation of $\langle \epsilon \rangle$ at these appropriate resolutions, are given in figure 18, and the errors are small when compared with the ratio of dissipation in the rough surface case to that in the smooth surface case.

Appendix B. Dependence on the forcing amplitude

Here, we analyse the role played by the amplitude of the incident wave in energy dissipation and mean flow. In figure 19, we plot $\langle \epsilon \rangle$ at $\sigma = h$ versus A^2 , and the data are from figure 18. It is clear that $\langle \epsilon \rangle_{\sigma=h}$ is proportional to the square of the wave amplitude. In figure 20, we plot the maximum mean flow velocity in the direction parallel to slope $V_s(\text{max})$ versus A^2 at different γ . For simplicity, λ is fixed at 0. Again, it is found that $V_s(\text{max})$ is proportional to A^2 .

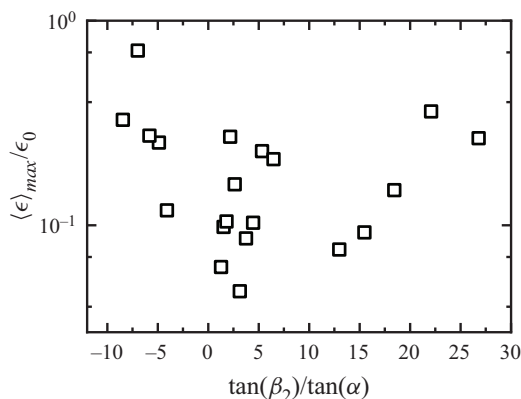


Figure 21. Maximum value in the averaged dissipation profile $(\epsilon)_{max}/\epsilon_0$ versus the criticality of the slopes of the roughness element. The data are taken from figure 13(a). The data in the smooth surface case are not used as there are no roughness elements.

Appendix C. Dependence on the criticality of the slopes of the roughness element

Figure 21 shows the maximum value in the averaged dissipation profile versus the criticality of the slopes of the roughness elements. The criticality is defined as $\tan(\beta_2)/\tan(\alpha)$, where β_2 is the angle between the right side of the roughness element and the horizontal, and α is the angle of the incident waves. One may see that the data points in the figure are very scattered, which means that the criticality of the slopes of the roughness elements seems not to be a good choice as a control parameter in this study. We would also like to emphasize that this criticality is not a independent variable as it is determined when the values of λ and γ are given.

REFERENCES

- ADRIAN, R.J. 1991 Particle-imaging techniques for experimental fluid mechanics. *Annu. Rev. Fluid Mech.* **23** (1), 261–304.
- ALFORD, M.H. 2003 Redistribution of energy available for ocean mixing by long-range propagation of internal waves. *Nature* **423** (6936), 159–162.
- ALFORD, M.H., *et al.* 2011 Energy flux and dissipation in Luzon Strait: two tales of two ridges. *J. Phys. Oceanogr.* **41** (11), 2211–2222.
- ALFORD, M.H. & ZHAO, Z. 2007 Global patterns of low-mode internal-wave propagation. Part I: energy and energy flux. *J. Phys. Oceanogr.* **37** (7), 1829–1848.
- ARTHUR, R.S., KOSEFF, J.R. & FRINGER, O.B. 2017 Local versus volume-integrated turbulence and mixing in breaking internal waves on slopes. *J. Fluid Mech.* **815**, 169–198.
- AUCAN, J., MERRIFIELD, M.A., LUTHER, D.S. & FLAMENT, P. 2006 Tidal mixing events on the deep flanks of Kaena Ridge, Hawaii. *J. Phys. Oceanogr.* **36** (6), 1202–1219.
- CACCHIONE, D. & WUNSCH, C. 1974 Experimental study of internal waves over a slope. *J. Fluid Mech.* **66** (2), 223–239.
- CARTER, G.S. & GREGG, M.C. 2006 Persistent near-diurnal internal waves observed above a site of M_2 barotropic-to-baroclinic conversion. *J. Phys. Oceanogr.* **36** (6), 1136–1147.
- CHALAMALLA, V.K., GAYEN, B., SCOTTI, A. & SARKAR, S. 2013 Turbulence during the reflection of internal gravity waves at critical and near-critical slopes. *J. Fluid Mech.* **729**, 47–68.
- ERIKSEN, C.C. 1982 Observations of internal wave reflection off sloping bottoms. *J. Geophys. Res.* **87** (C1), 525–538.
- FORTUIN, J.M.H. 1960 Theory and application of two supplementary methods of constructing density gradient columns. *J. Polym. Sci.* **44** (144), 505–515.
- GILBERT, D. & GARRETT, C. 1989 Implications for ocean mixing of internal wave scattering off irregular topography. *J. Phys. Oceanogr.* **19** (11), 1716–1729.

Internal gravity waves incident upon rough slopes

- GOSTIAUX, L., DAUXOIS, T., DIDELLE, H., SOMMERIA, J. & VIBOUD, S. 2006 Quantitative laboratory observations of internal wave reflection on ascending slopes. *Phys. Fluids* **18** (5), 056602.
- GRISOUARD, N. 2010 Réflexions non-linéaires d'ondes de gravité internes. PhD thesis, Université de Grenoble.
- HALL, R.A., HUTHNANCE, J.M. & WILLIAMS, R.G. 2013 Internal wave reflection on shelf slopes with depth-varying stratification. *J. Phys. Oceanogr.* **43** (2), 248–258.
- HURLEY, D.G. & KEADY, G. 1997 The generation of internal waves by vibrating elliptic cylinders. Part 2. Approximate viscous solution. *J. Fluid Mech.* **351**, 119–138.
- IVEY, G.N. & NOKES, R.I. 1989 Vertical mixing due to the breaking of critical internal waves on sloping boundaries. *J. Fluid Mech.* **204**, 479–500.
- IVEY, G.N., WINTERS, K.B. & DE SILVA, I.P.D. 2000 Turbulent mixing in a sloping benthic boundary layer energized by internal waves. *J. Fluid Mech.* **418**, 59–76.
- JOHNSTON, T.M.S., RUDNICK, D.L., CARTER, G.S., TODD, R.E. & COLE, S.T. 2011 Internal tidal beams and mixing near Monterey Bay. *J. Geophys. Res.: Oceans* **116**, C03017.
- KATAOKA, T. & AKYLAS, T.R. 2020 Viscous reflection of internal waves from a slope. *Phys. Rev. Fluids* **5** (1), 014803.
- KELL, G.S. 1975 Density, thermal expansivity, and compressibility of liquid water from 0° to 150°C: correlations and tables for atmospheric pressure and saturation reviewed and expressed on 1968 temperature scale. *J. Chem. Engng Data* **20** (1), 97–105.
- KLYMAK, J.M., MOUM, J.N., NASH, J.D., KUNZE, E., GIRTON, J.B., CARTER, G.S., LEE, C.M., SANFORD, T.B. & GREGG, M.C. 2006 An estimate of tidal energy lost to turbulence at the Hawaiian Ridge. *J. Phys. Oceanogr.* **36** (6), 1148–1164.
- KLYMAK, J.M., PINKEL, R. & RAINVILLE, L. 2008 Direct breaking of the internal tide near topography: Kaena Ridge, Hawaii. *J. Phys. Oceanogr.* **38** (2), 380–399.
- KUNZE, E. & LLEWELLYN SMITH, S.G. 2004 The role of small-scale topography in turbulent mixing of the global ocean. *Oceanography* **17** (1), 55–64.
- KUNZE, E., MACKAY, C., MCPHEE-SHAW, E.E., MORRICE, K., GIRTON, J.B. & TERKER, S.R. 2012 Turbulent mixing and exchange with interior waters on sloping boundaries. *J. Phys. Oceanogr.* **42** (6), 910–927.
- LAMB, K.G. 2014 Internal wave breaking and dissipation mechanisms on the continental slope/shelf. *Annu. Rev. Fluid Mech.* **46** (1), 231–254.
- LEDWELL, J.R., MONTGOMERY, E.T., POLZIN, K.L., ST. LAURENT, L.C., SCHMITT, R.W. & TOOLE, J.M. 2000 Evidence for enhanced mixing over rough topography in the Abyssal Ocean. *Nature* **403** (6766), 179–182.
- LEE, C.M., SANFORD, T.B., KUNZE, E., NASH, J.D., MERRIFIELD, M.A. & HOLLOWAY, P.E. 2006 Internal tides and turbulence along the 3000-m isobath of the Hawaiian Ridge. *J. Phys. Oceanogr.* **36** (6), 1165–1183.
- LEGG, S. 2004 Internal tides generated on a corrugated continental slope. Part I: cross-slope barotropic forcing. *J. Phys. Oceanogr.* **34** (1), 156–173.
- LEGG, S. 2014 Scattering of low-mode internal waves at finite isolated topography. *J. Phys. Oceanogr.* **44** (1), 359–383.
- LEGG, S. & ADCROFT, A. 2003 Internal wave breaking at concave and convex continental slopes. *J. Phys. Oceanogr.* **33** (11), 2224–2246.
- LEVINE, M.D. & BOYD, T.J. 2006 Tidally forced internal waves and overturns observed on a slope: results from home. *J. Phys. Oceanogr.* **36** (6), 1184–1201.
- LIGHTHILL, J. 1978 *Waves in Fluids*. Cambridge University Press.
- LONGUET-HIGGINS, M.S. 1969 On the reflexion of wave characteristics from rough surfaces. *J. Fluid Mech.* **37** (2), 231–250.
- MARTINI, K., ALFORD, M., KUNZE, E., KELLY, S. & NASH, J. 2011 Observations of internal tides on the Oregon continental slope. *J. Phys. Oceanogr.* **41** (9), 1772–1794.
- MIED, R.P. & DUGAN, J.P. 1976 Internal wave reflexion from a sinusoidally corrugated surface. *J. Fluid Mech.* **76** (2), 259–272.
- MÜLLER, P. & LIU, X.B. 2000a Scattering of internal waves at finite topography in two dimensions. Part I: theory and case studies. *J. Phys. Oceanogr.* **30** (3), 532–549.
- MÜLLER, P. & LIU, X.B. 2000b Scattering of internal waves at finite topography in two dimensions. Part II: spectral calculations and boundary mixing. *J. Phys. Oceanogr.* **30** (3), 550–563.
- MUNK, W. & WUNSCH, C. 1998 Abyssal recipes II: energetics of tidal and wind mixing. *Deep-Sea Res.* (1) **45** (12), 1977–2010.
- NAKAMURA, T. & AWAJI, T. 2009 Scattering of internal waves with frequency change over rough topography. *J. Phys. Oceanogr.* **39** (7), 1574–1594.

- NASH, J., ALFORD, M., KUNZE, E., MARTINI, K. & KELLEY, S. 2007 Hotspots of deep ocean mixing on the Oregon continental slope. *Geophys. Res. Lett.* **34** (1), L01605.
- NASH, J., KUNZE, E., TOOLE, J. & SCHMITT, R. 2004 Internal tide reflection and turbulent mixing on the continental slope. *J. Phys. Oceanogr.* **34** (5), 1117–1134.
- NAZARIAN, R.H. & LEGG, S. 2017a Internal wave scattering in continental slope canyons, part 1: theory and development of a ray tracing algorithm. *Ocean Model.* **118**, 1–15.
- NAZARIAN, R.H. & LEGG, S. 2017b Internal wave scattering in continental slope canyons, part 2: a comparison of ray tracing and numerical simulations. *Ocean Model.* **118**, 16–30.
- NIKURASHIN, M. & LEGG, S. 2011 A mechanism for local dissipation of internal tides generated at rough topography. *J. Phys. Oceanogr.* **41** (2), 378–395.
- POPE, S.B. 2000 *Turbulent Flows*. Cambridge University Press.
- RAY, R. & MITCHUM, G. 1996 Surface manifestation of internal tides generated near Hawaii. *Geophys. Res. Lett.* **23** (16), 2101–2104.
- RODENBORN, B., KIEFER, D., ZHANG, H.P. & SWINNEY, H.L. 2011 Harmonic generation by reflecting internal waves. *Phys. Fluids* **23** (2), 026601.
- SARKAR, S. & SCOTTI, A. 2017 From topographic internal gravity waves to turbulence. *Annu. Rev. Fluid Mech.* **49**, 195–220.
- SCOTTI, A. 2011 Inviscid critical and near-critical reflection of internal waves in the time domain. *J. Fluid Mech.* **674**, 464–488.
- ST. LAURENT, L. & GARRETT, C. 2002 The role of internal tides in mixing the deep ocean. *J. Phys. Oceanogr.* **32** (10), 2882–2899.
- SUTHERLAND, B.R. 2010 *Internal Gravity Waves*. Cambridge University Press.
- SUTHERLAND, B.R., DALZIEL, S.B., HUGHES, G.O. & LINDEN, P.F. 1999 Visualization and measurement of internal waves by ‘synthetic schlieren’. Part 1. Vertically oscillating cylinder. *J. Fluid Mech.* **390**, 93–126.
- TAYLOR, J.R. 1993 Turbulence and mixing in the boundary layer generated by shoaling internal waves. *Dyn. Atmos. Oceans* **19** (1–4), 233–258.
- THORPE, S.A. 2001 Internal wave reflection and scatter from sloping rough topography. *J. Phys. Oceanogr.* **31** (2), 537–553.
- THORPE, S.A. & HAINES, A.P. 1987 On the reflection of a train of finite-amplitude internal waves from a uniform slope. *J. Fluid Mech.* **178**, 279–302.
- TOKGOZ, S., ELSINGA, G.E., DELFOS, R. & WESTERWEEEL, J. 2012 Spatial resolution and dissipation rate estimation in Taylor–Couette flow for tomographic PIV. *Exp. Fluids* **53** (3), 561–583.
- WEBB, P. 2019 Introduction to oceanography. <https://open.umn.edu/opentextbooks/textbooks/introduction-to-oceanography>.
- WUNSCH, C. & FERRARI, R. 2004 Vertical mixing, energy, and the general circulation of the oceans. *Annu. Rev. Fluid Mech.* **36** (1), 281–314.
- XIA, K.-Q., SUN, C. & ZHOU, S.Q. 2003 Particle image velocimetry measurement of the velocity field in turbulent thermal convection. *Phys. Rev. E* **68** (6), 066303.
- ZHANG, H.P., KING, B. & SWINNEY, H.L. 2007 Experimental study of internal gravity waves generated by supercritical topography. *Phys. Fluids* **19** (9), 096602.
- ZHAO, Z., ALFORD, M. & MACKINNON, J. 2010 Long-range propagation of the semi-diurnal internal tide from the Hawaiian Ridge. *J. Phys. Oceanogr.* **40** (4), 713–736.